


 Cite this: *RSC Adv.*, 2025, 15, 39355

# One-step electrodeposition of W, Mo-Ni<sub>3</sub>S<sub>2</sub>/NF catalyst: an efficient hydrogen evolution electrode for alkaline media

 Wenyu Tan  and Hanwei He\*

A self-supported tungsten (W), molybdenum (Mo)-Ni<sub>3</sub>S<sub>2</sub>/nickel foam (NF) hydrogen evolution reaction (HER) electrode was successfully fabricated on NF *via* constant current electrodeposition. The morphology, elemental composition, and electrocatalytic HER performance of the electrodes were systematically characterized *via* scanning electron microscopy, transmission electron microscopy, X-ray diffraction, and an electrochemical workstation. Results indicate that the surface of the W, Mo-Ni<sub>3</sub>S<sub>2</sub>/NF electrode consists of rough and refined nano-spherical particles with certain amorphous characteristics. In 1 M KOH, the W, Mo-Ni<sub>3</sub>S<sub>2</sub>/NF electrode demonstrates superior catalytic HER activity and stability. In particular, it achieves an overpotential of only 76 mV at a current density of 10 mA cm<sup>-2</sup>. After undergoing 2000 cyclic voltammetry cycles and 12 h of continuous electrolysis, the electrode retains its high HER activity. The nano-spherical morphology and coexistence of amorphous/crystalline structures significantly enhance the electrochemical active surface area and expose more catalytic active sites. Moreover, the incorporation of W and Mo effectively modulates the electronic structure of Ni<sub>3</sub>S<sub>2</sub>, reducing charge transfer resistance, and consequently, enhancing the overall HER catalytic performance of the electrode.

Received 26th September 2025

Accepted 15th October 2025

DOI: 10.1039/d5ra07318a

[rsc.li/rsc-advances](https://rsc.li/rsc-advances)

## 1. Introduction

As one of the clean energy sources, hydrogen (H) gas (H<sub>2</sub>) has garnered significant attention in the transition away from traditional fossil fuels due to its high energy density, renewability, and zero emissions.<sup>1</sup> Among various H<sub>2</sub> production technologies, water electrolysis stands out because of its abundant raw material (H<sub>2</sub>O), high conversion efficiency, and environmental friendliness, leading to rapid advancements and extensive research in the green H sector. However, owing to cathode polarization, solution resistance, and contact resistance, a higher applied potential is still required to overcome the reaction energy barrier during practical H<sub>2</sub> production *via* water electrolysis.<sup>2</sup> Although platinum (Pt)-based catalysts exhibit superior performance in H evolution reaction (HER), their scarcity and high cost necessitate the development of non-noble metal catalysts that exhibit high intrinsic activity and long-term durability.<sup>3</sup>

Nickel (Ni)-based sulfide electrocatalysts are highly promising for alkaline HER in water electrolysis. Ni atoms possess unpaired 3d electrons in their outer shell, which can readily hybridize with 1s orbital electrons of H atoms to form metal-H bonds, promoting the adsorption of the reaction intermediate H<sub>ads</sub>.<sup>4</sup> In addition, the relatively high electronegativity of sulfur

(S) atoms, upon forming a composite with the transition metal Ni, effectively reduces the electron density of Ni atoms. This phenomenon weakens the binding strength of metal-H<sub>ads</sub>, facilitating the desorption of H and ultimately enhancing electrocatalytic performance. For example, Mahanthappa *et al.*<sup>5</sup> developed NiS-NiS<sub>2</sub> electrodes supported on layered porous S-doped graphitic carbon (C) nitride (SGCN) nanosheets as bifunctional catalysts. These electrodes achieved an overall water splitting current density of 50 mA cm<sup>-2</sup> at a low cell voltage of 1.66 V. Their study revealed that Ni<sup>2+</sup>/Ni<sup>3+</sup> acted as redox active centers, and the interface between NiS-NiS<sub>2</sub> and SGCN nanosheets featured abundant S vacancies and strong electronic coupling. Doping other elements into Ni-based sulfide catalysts is an effective strategy for further enhancing their electrocatalytic activity. For example, Fathollahi *et al.*<sup>6</sup> fabricated porous Ni-Fe-S nanosheets on Ni foam (NF) substrates *via* the dynamic H bubble template method. These nanosheets exhibited an overpotential of 85 mV and 173 mV at a current density of 10 mA cm<sup>-2</sup> and 100 mA cm<sup>-2</sup>, respectively. The incorporation of iron (Fe) and S played a critical role in boosting HER catalytic performance. This optimization arose from the chemical interactions and structural reconfigurations of metal-S bonds, wherein the electronegativity of S dominates the bonding properties, while Fe doping modulates the electronic structure.

As non-noble metal alkaline electrolytic water catalysts, Ni-Mo-based electrodes exhibit significant potential. Bau *et al.*<sup>7</sup>

Powder Metallurgy Research Institute, Central South University, Changsha 410083, China. E-mail: hehanwei@csu.edu.cn



conducted a combined experimental and theoretical study, revealing the dominant role of  $\text{Mo}^{3+}$  ions in enhancing HER performance. Their theoretical simulations showed that upon the incorporation of  $\text{Mo}^{3+}$  active centers onto Ni(111) surface, the system exhibited excellent thermodynamic stability and markedly improved catalytic activity within the HER potential range. Moreover, electron transfer occurred from the Ni surface to the molybdenum (Mo) surface upon alloy formation due to the higher electronegativity of Mo compared with that of Ni. This redistribution of electrons modified the electronic structure, leading to an optimal proton binding energy that facilitated efficient HER performance.<sup>8,9</sup> Yang *et al.*<sup>10</sup> employed *in situ* variable-temperature near ambient pressure X-ray photoelectron spectroscopy (XPS) technology to systematically investigate the formation mechanism of the  $\text{WNi}_4@/\text{WO}_2$  heterostructure. They found that the electronic interaction between tungsten (W) and Ni optimized  $\text{H}^*$  adsorption energy. In addition, the alloy structure offered more active sites, providing a new idea for doping other elements for a Ni-based sulfide electrode. Based on these research outcomes, the current study introduced W and Mo into the  $\text{Ni}_3\text{S}_2/\text{NF}$  electrode to fabricate a W, Mo co-doped  $\text{Ni}_3\text{S}_2/\text{NF}$  electrocatalyst and then comprehensively evaluated its HER catalytic performance and mechanisms. Compared with chemical synthesis methods, such as hydrothermal<sup>11</sup> or high-temperature solid-phase synthesis,<sup>12</sup> which involve preparing catalytically active materials and subsequently coating them onto substrates, electrodeposition directly deposits catalytically active materials onto the substrate to prepare self-supporting electrodes.<sup>13</sup> This method not only simplifies the operational process and enhances controllability but also effectively reduces contact resistance between the catalytically active material and the substrate, improving the electrical conductivity of the electrode and enhancing its long-term stability.

In the current study, the self-supported W, Mo- $\text{Ni}_3\text{S}_2/\text{NF}$  electrode was successfully synthesized on NF substrate *via* a one-step constant current electrodeposition method. The incorporation of W and Mo not only optimized the morphology of the electrode but also modulated electron distribution around Ni and S atoms, enhancing its catalytic performance. The W, Mo- $\text{Ni}_3\text{S}_2/\text{NF}$  electrocatalyst exhibited an overpotential of 76 mV at a current density of  $10 \text{ mA cm}^{-2}$  and a Tafel slope of  $125.7 \text{ mV dec}^{-1}$ . In addition, the W, Mo- $\text{Ni}_3\text{S}_2/\text{NF}$  electrode demonstrated excellent mechanical robustness and long-term electrochemical stability. The current study presents a novel and efficient strategy for fabricating non-noble metal catalysts under alkaline conditions by using a simple electrodeposition method.

## 2. Experimental

### 2.1 Reagents

The NF substrate was purchased from Kunshan Desco Electronics Co., Ltd (Jiangsu, China), and the high-purity N was obtained from Changsha Ruichong Gas Co., Ltd (Hunan, China). The 20% Pt/C and 5 wt% Nafion used to prepare the Pt/C electrode were purchased from Sigma-Aldrich Reagent

Company, USA. All the other reagents, including Ni sulfate hydrate ( $\text{NiSO}_4 \cdot 6\text{H}_2\text{O}$ ), sodium (Na) molybdate ( $\text{Na}_2\text{MoO}_4 \cdot 2\text{H}_2\text{O}$ ), Na tungstate ( $\text{Na}_2\text{WO}_4 \cdot 2\text{H}_2\text{O}$ ), thiourea ( $\text{CH}_4\text{N}_2\text{S}$ ), Na citrate ( $\text{Na}_3\text{C}_6\text{H}_5\text{O}_7 \cdot 2\text{H}_2\text{O}$ ), Na chloride (NaCl), boric acid ( $\text{H}_3\text{BO}_3$ ), potassium (K) hydroxide (KOH), and hydrochloric acid (HCl), were procured from Shanghai Sinopharm Chemical Co., Ltd (Shanghai, China). All the reagents were of analytical grade and could be used directly.

### 2.2 Preparation method

**2.2.1 Preprocessing of NF.** Before electrodeposition, a NF cutting that measured  $1 \text{ cm} \times 1 \text{ cm} \times 0.03 \text{ cm}$  (with reserved tabs) was sequentially ultrasonicated in acetone and ethanol for 10 min each to remove surface organic contaminants. Subsequently, it was washed with deionized water and further ultrasonicated in 10 wt% HCl for 20 min to eliminate surface oxides and activate the NF surface. The foam was then repeatedly rinsed with deionized water until the pH of the rinse solution reached 7. Finally, the foam was vacuum-dried at  $50 \text{ }^\circ\text{C}$  for 8 h.

**2.2.2 W, Mo- $\text{Ni}_3\text{S}_2/\text{NF}$  electrocatalyst.** Electrodeposition was performed on a CHI660E electrochemical workstation. The electrolyte solution used to prepare the  $\text{Ni}_3\text{S}_2/\text{NF}$  electrode consisted of  $100 \text{ g L}^{-1}$  of  $\text{NiSO}_4 \cdot 6\text{H}_2\text{O}$ ,  $100 \text{ g L}^{-1}$  of  $\text{CH}_4\text{N}_2\text{S}$ ,  $70 \text{ g L}^{-1}$  of  $\text{Na}_3\text{C}_6\text{H}_5\text{O}_7 \cdot 2\text{H}_2\text{O}$ ,  $20 \text{ g L}^{-1}$  of NaCl, and  $40 \text{ g L}^{-1}$  of  $\text{H}_3\text{BO}_3$ . The pH of the solution was adjusted to 4.0 by using 10 wt% HCl. Electrodeposition was conducted at  $40 \text{ }^\circ\text{C}$  in a water bath under a constant current density of  $30 \text{ mA cm}^{-2}$  for 60 min. After deposition, the samples were sequentially washed with acetone, anhydrous ethanol, and deionized water to remove any residual electrolyte, followed by vacuum drying at  $50 \text{ }^\circ\text{C}$  for 6 h.

The preparation process of W, Mo- $\text{Ni}_3\text{S}_2/\text{NF}$  was basically the same as that of  $\text{Ni}_3\text{S}_2/\text{NF}$ , with the only difference being the addition of  $\text{Na}_2\text{WO}_4 \cdot 2\text{H}_2\text{O}$  and  $\text{Na}_2\text{MoO}_4 \cdot 2\text{H}_2\text{O}$  to the plating solution. The W- $\text{Ni}_3\text{S}_2/\text{NF}$  and Mo- $\text{Ni}_3\text{S}_2/\text{NF}$  used as control electrodes were prepared by adding  $\text{Na}_2\text{WO}_4 \cdot 2\text{H}_2\text{O}$  and  $\text{Na}_2\text{MoO}_4 \cdot 2\text{H}_2\text{O}$  to the electrolyte, respectively. Table 1 summarizes the composition of the electrolyte and the electrodeposition conditions employed in the preparation of the aforementioned electrocatalysts. Fig. 1 illustrates the synthesized process of the W, Mo- $\text{Ni}_3\text{S}_2/\text{NF}$  electrocatalyst. The mass loading of the W- $\text{Ni}_3\text{S}_2/\text{NF}$ , Mo- $\text{Ni}_3\text{S}_2/\text{NF}$  and W, Mo- $\text{Ni}_3\text{S}_2/\text{NF}$  electrocatalyst are approximately 4.1, 3.7 and  $3.8 \text{ mg cm}^{-2}$ , respectively.

**2.2.3 Pt/C electrode.** The ink was prepared by mixing 8 mg of 20% Pt/C powder with 80  $\mu\text{L}$  of 5 wt% Nafion, 460  $\mu\text{L}$  of anhydrous ethanol, and 460  $\mu\text{L}$  of deionized water. The ink was then sonicated in an ice bath for 1 h to ensure uniform dispersion. Subsequently, 35  $\mu\text{L}$  of the ink was evenly cast onto the surface of a glassy C electrode (GCE), which was then placed horizontally under an infrared lamp and dried for 3–5 min prior to measurement. The resulting catalyst loading on the GCE surface was  $1 \text{ mg cm}^{-2}$ .

### 2.3 Characterization

The microstructure and elemental composition distribution of the W, Mo- $\text{Ni}_3\text{S}_2/\text{NF}$  electrocatalyst were characterized *via*



**Table 1** Electrodeposition parameters and electrolyte composition of Ni<sub>3</sub>S<sub>2</sub>/NF, W-Ni<sub>3</sub>S<sub>2</sub>/NF, Mo-Ni<sub>3</sub>S<sub>2</sub>/NF and W, Mo-Ni<sub>3</sub>S<sub>2</sub>/NF electrodes

	Ni <sub>3</sub> S <sub>2</sub> /NF	W-Ni <sub>3</sub> S <sub>2</sub> /NF	Mo-Ni <sub>3</sub> S <sub>2</sub> /NF	W, Mo-Ni <sub>3</sub> S <sub>2</sub> /NF
NiSO <sub>4</sub> ·6H <sub>2</sub> O (g L <sup>-1</sup> )	100	100	100	100
CH <sub>4</sub> N <sub>2</sub> S (g L <sup>-1</sup> )	100	100	100	100
Na <sub>3</sub> C <sub>6</sub> H <sub>5</sub> O <sub>7</sub> ·2H <sub>2</sub> O (g L <sup>-1</sup> )	70	70	70	70
Na <sub>2</sub> WO <sub>4</sub> ·2H <sub>2</sub> O (g L <sup>-1</sup> )	—	10	—	10
Na <sub>2</sub> MoO <sub>4</sub> ·2H <sub>2</sub> O (g L <sup>-1</sup> )	—	—	30	30
NaCl (g L <sup>-1</sup> )	20	20	20	20
H <sub>3</sub> BO <sub>3</sub> (g L <sup>-1</sup> )	40	40	40	40
pH	4.0	4.0	4.0	4.0
Current density (mA cm <sup>-2</sup> )	30	30	30	30
Time (min)	60	60	60	60
Temperature (°C)	40	40	40	40

transmission electron microscopy (TEM) with a JEM-F200 multipurpose electron microscope (JEOL Ltd, Japan), scanning electron microscopy (SEM) with a MIRA4 LMH field-emission scanning electron microscope (TESCAN Ltd, CZ), and energy-dispersive X-ray spectroscopy (EDS) with an Ultim Max 65 EDS detector (Oxford Instruments, UK). The crystal structure of the samples was analyzed *via* X-ray diffraction (XRD) by using a SmartLab SE multipurpose X-ray diffractometer (Rigaku, Japan) with a Cu K<sub>α</sub> radiation source (wavelength: 0.1541 nm), operating at tube voltage of 40 kV and tube current of 40 mA, with a scanning rate of 5° min<sup>-1</sup>. The elemental composition and chemical states on the surface of the electrocatalyst were analyzed *via* X-ray photoelectron spectroscopy (XPS) by using a K-Alpha X-ray photoelectron spectrometer (Thermo Fisher Scientific Inc., USA) with an aluminum target ( $h\nu = 1486.6$  eV) employed during the measurements.

#### 2.4 Electrochemical methods

Electrochemical measurements were performed using a CHI660E electrochemical workstation with a standard three-electrode system. A 100 mL glass electrolytic cell was employed for the tests. The H evolution performance of the electrodes was evaluated at room temperature (25 °C, 1 M KOH). Prior to testing, high-purity N<sub>2</sub> was bubbled through the electrolyte for 10 min to remove dissolved O<sub>2</sub>, and the entire three-electrode system was immersed in the electrolyte for 3 min to ensure stabilization. The prepared electrode, graphite

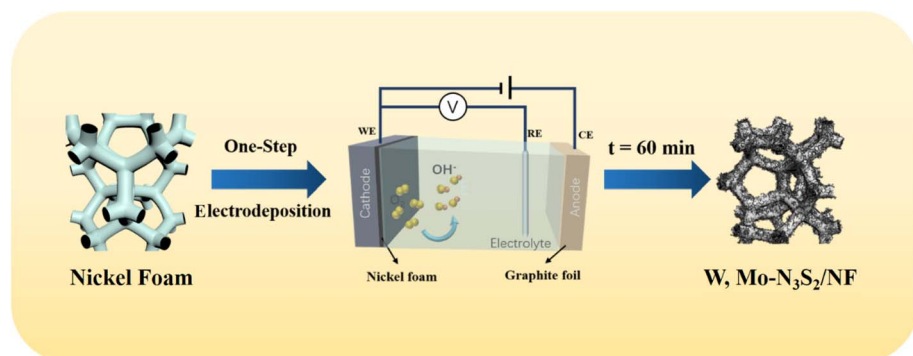
electrode, and saturated calomel electrode (SCE) served as the working electrode, counter electrode, and reference electrode, respectively. To facilitate potential comparison, all potentials were converted into the reversible H electrode (RHE;  $E_{vs.RHE}$ ) potential by using the Nernst equation:<sup>14</sup>

$$E_{vs.RHE} = E_{vs.SCE} + 0.242 + 0.059 \times \text{pH} - 0.000791 \times (T - 298.15) - iR. \quad (1)$$

In this study, the polarization curve was recorded within the potential range of  $E_{vs.SCE}$  from 0 V to -1.6 V at a scan rate of 2 mV s<sup>-1</sup>. The double-layer capacitance ( $C_{dl}$ ) of the electrocatalyst was determined *via* cyclic voltammetry (CV) with scan rates that ranged from 10 mV s<sup>-1</sup> to 100 mV s<sup>-1</sup> in the non-faradaic region. To evaluate the cycling stability of the samples, 2000 CV cycles were performed within the potential window of  $E_{vs.SCE}$  from -0.2 V to -0.6 V. The charge transfer efficiency of the electrode was assessed *via* electrochemical impedance spectroscopy. Chronopotentiometry (CP) curves were employed to investigate the electrochemical stability of the electrocatalyst under various current density conditions.

### 3. Results and discussion

The XRD patterns are presented in Fig. 2. As illustrated in Fig. 2(a), the Ni<sub>3</sub>S<sub>2</sub>/NF electrode exhibits distinct diffraction peaks at  $2\theta = 44.4^\circ$ ,  $51.8^\circ$ , and  $76.3^\circ$ , which correspond to the

**Fig. 1** Schematic illustration of the preparing process of W, Mo-Ni<sub>3</sub>S<sub>2</sub>/NF electrode.

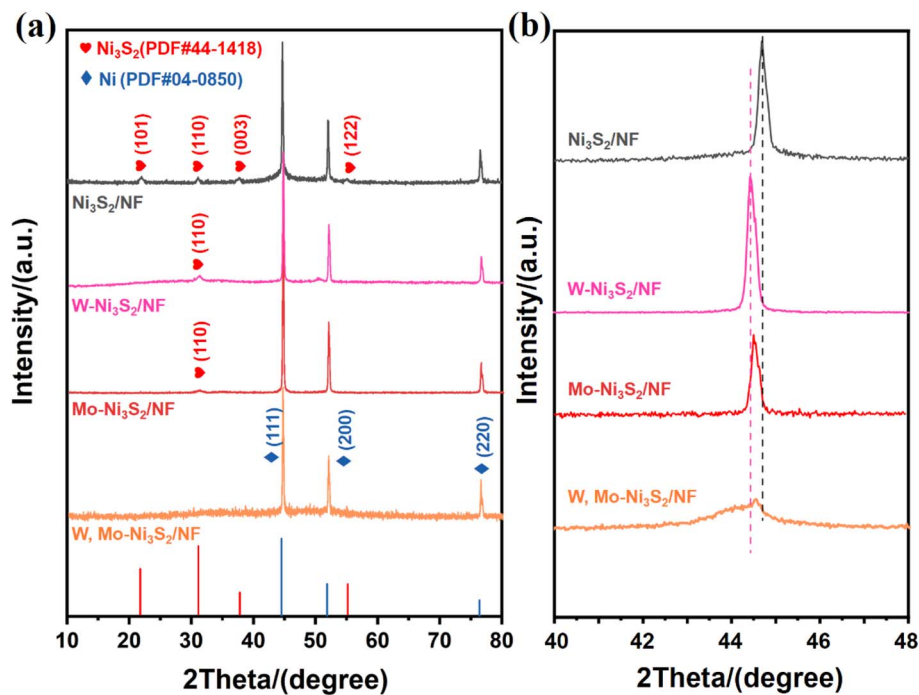


Fig. 2 (a) XRD patterns of  $\text{Ni}_3\text{S}_2/\text{NF}$ ,  $\text{W-Ni}_3\text{S}_2/\text{NF}$ ,  $\text{Mo-Ni}_3\text{S}_2/\text{NF}$  and  $\text{W, Mo-Ni}_3\text{S}_2/\text{NF}$  electrodes; (b) partial magnification of XRD patterns.

(111), (200), and (220) crystal planes of Ni, respectively (JCPDS 04-0850).<sup>15</sup> This phenomenon may be attributed to the relatively thin catalytic layer formed during deposition. In addition, the diffraction peaks located at  $21.7^\circ$ ,  $31.1^\circ$ ,  $37.7^\circ$ , and  $55.1^\circ$  are associated with the (101), (110), (003), and (122) crystal planes of  $\text{Ni}_3\text{S}_2$ , respectively (JCPDS 44-1418).<sup>16</sup> The presence of the  $\text{Ni}_3\text{S}_2$  phase, which is an excellent H evolution catalyst, significantly enhances the H evolution catalytic activity of the electrode.<sup>17</sup> Moreover, the broadened diffraction peaks suggest a certain degree of amorphization in the electrode structure. In addition to the three main peaks of Ni, the XRD patterns of  $\text{W-Ni}_3\text{S}_2/\text{NF}$  and  $\text{Mo-Ni}_3\text{S}_2/\text{NF}$  exhibit a diffraction peak that corresponds to the (110) crystal plane of  $\text{Ni}_3\text{S}_2$  at  $31.7^\circ$ . For the  $\text{W, Mo-Ni}_3\text{S}_2/\text{NF}$  electrode, the degree of peak broadening is enhanced, indicating more pronounced amorphous characteristics. No phases that contain W or Mo are found in the pattern, because W and Mo atoms have substituted some Ni atoms into the lattice, forming a substitutional solid solution,<sup>18</sup> which is difficult to characterize *via* XRD. The atomic radius of W or Mo are larger than that of Ni, as shown in the magnified view of Fig. 2(b). This substitution induces lattice distortion and expansion, leading to a shift of the diffraction peaks toward smaller angles.<sup>19</sup> The atomic radius of W is slightly larger than that of Mo, and thus, the negative angle shift of the diffraction peak in the  $\text{W-Ni}_3\text{S}_2/\text{NF}$  pattern is the most significant, while those of  $\text{Mo-Ni}_3\text{S}_2/\text{NF}$  and  $\text{W, Mo-Ni}_3\text{S}_2/\text{NF}$  fall between  $\text{W-Ni}_3\text{S}_2/\text{NF}$  and  $\text{Ni}_3\text{S}_2/\text{NF}$ . Fig. S1 also illustrates the crystal structure of  $\text{Ni}_3\text{S}_2$ , where Ni atoms occupy two distinct crystallographic positions and form octahedral and tetrahedral coordination with S atoms, while S atoms connect to Ni atoms *via* bridging or terminal bonding to form layered or chain-like structural units.<sup>20</sup>

Fig. S2 presents the SEM image of NF, clearly illustrating a smooth foam-like structure. As shown in Fig. 3(a and b), the surface of  $\text{Ni}_3\text{S}_2/\text{NF}$  exhibits a cellular morphology with minimal undulation. Upon introducing W, however, the electrode surface transitions from a relatively flat planar interface to a rough surface characterized by island-like protrusions, with more pronounced gaps between nanoparticles. This phenomenon arises because the valence electrons of transition elements possess empty orbitals, enabling Ni and W metal ions to form complexes in the presence of chelating agents (*e.g.*, Cit). Consequently, the initially disparate deposition potentials become closer, leading to induced co-deposition. The deposition process is completed within a relatively short period and followed by concurrent growth. Consequently, a cellular structure forms on the electrode surface, leading to increased roughness.<sup>21</sup> Fig. 3(c) presents the SEM image of the  $\text{Mo-Ni}_3\text{S}_2/\text{NF}$  electrode. Upon introducing Mo, a dense nanoparticle structure forms on the surface of the electrocatalyst. This phenomenon may be attributed to the relatively high electronegativity of Mo, which enables an appropriate concentration of Mo ions in the electrolyte to accelerate the reduction process. Consequently, the nucleation rate of crystal nuclei exceeds their growth rate, leading to grain refinement.<sup>22</sup> Consistent with the aforementioned discussion, the surface of the  $\text{W, Mo-Ni}_3\text{S}_2/\text{NF}$  electrocatalyst in Fig. 3(d) is relatively rough and features a layer of nano-spherical particle deposits, which increased the area of exposed nanostructures. Such a surface morphology offers abundant active sites for the HER process, facilitates direct contact between the electrolyte and the electrode material, promotes faster ion transport and exchange along the diffusion path, and thus, enhances the H



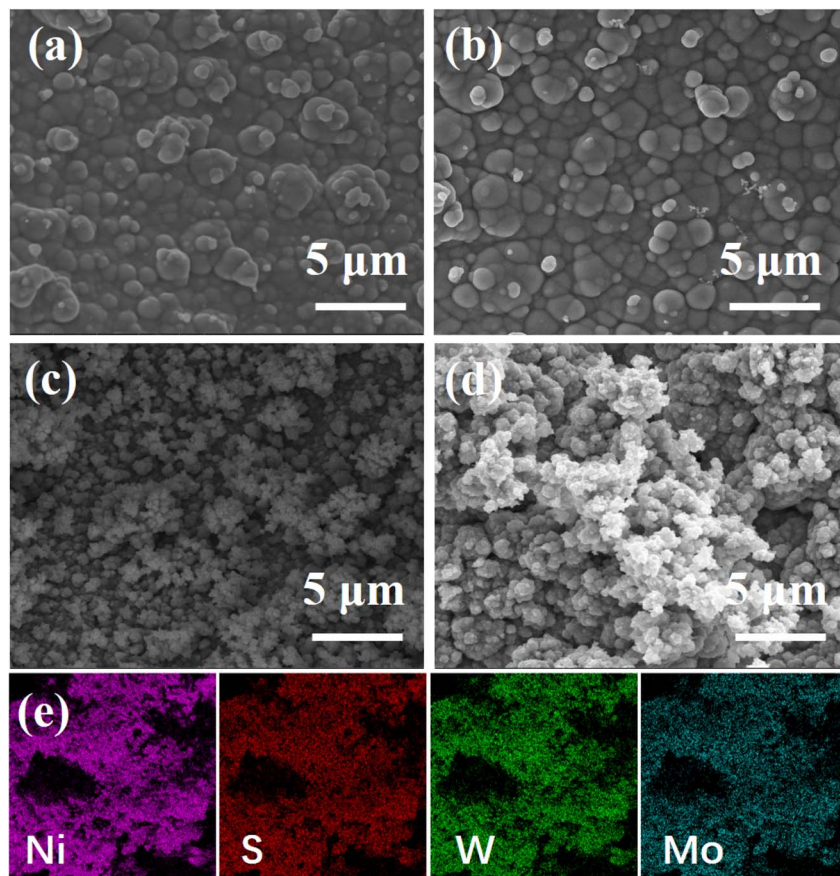


Fig. 3 SEM images of (a) Ni<sub>3</sub>S<sub>2</sub>/NF, (b) W-Ni<sub>3</sub>S<sub>2</sub>/NF, (c) Mo-Ni<sub>3</sub>S<sub>2</sub>/NF, and (d) W, Mo-Ni<sub>3</sub>S<sub>2</sub>/NF electrodes; (e) the corresponding elemental mappings of W, Mo-Ni<sub>3</sub>S<sub>2</sub>/NF electrode.

evolution catalytic activity of the electrocatalyst.<sup>23</sup> In addition, the elemental mapping in Fig. 3(e) confirms the uniform distribution of Ni, S, W, and Mo on the surface of the

electrocatalyst, verifying the successful synthesis of W, Mo-Ni<sub>3</sub>S<sub>2</sub>/NF. The corresponding elemental composition and content are presented in Fig. S3.

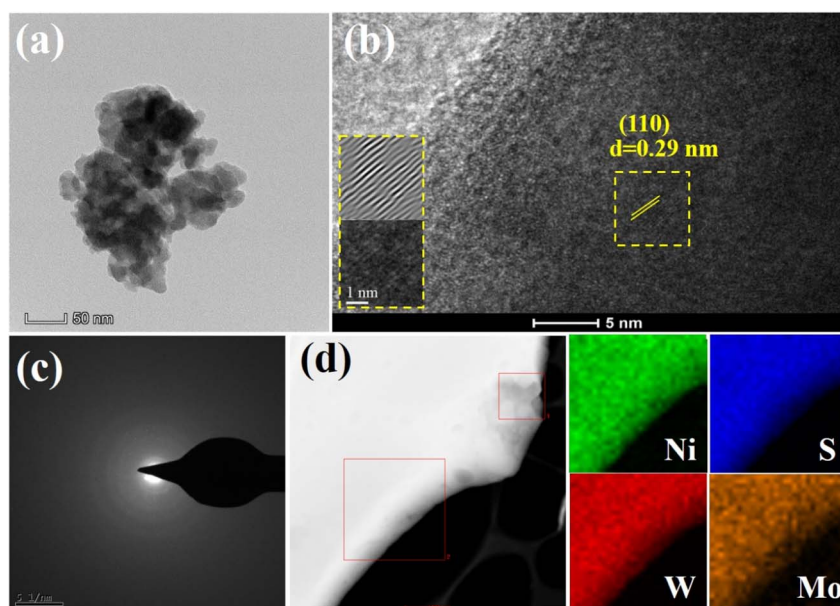


Fig. 4 (a) TEM image, (b) HRTEM image, (c) SAED result and (d) the corresponding elemental mappings of W, Mo-Ni<sub>3</sub>S<sub>2</sub>/NF electrode.



To investigate microscopic morphology and structural characteristics, the W, Mo-Ni<sub>3</sub>S<sub>2</sub>/NF electrode was analyzed *via* TEM, as illustrated in Fig. 4. W, Mo-Ni<sub>3</sub>S<sub>2</sub>/NF consists of numerous stacked nanospheres, with rough edges that enhance the contact area with the electrolyte [Fig. 4(a)], which is consistent with the SEM results. In the high-resolution TEM image [Fig. 4(b)], the lattice fringes are relatively indistinct, and the fringe spacing of  $d = 0.29$  nm corresponds to the (110) crystal plane of Ni<sub>3</sub>S<sub>2</sub>.<sup>24</sup> This phenomenon indicates the presence of a nanocrystalline Ni<sub>3</sub>S<sub>2</sub> phase within the electrode, along with a relatively high degree of amorphization. Fig. 4(c) further corroborates this result. The presence of nanocrystals leads to relatively sharp diffraction rings in the selected area electron diffraction pattern, while the typical amorphous halo ring pattern remains evident. In addition, the mapping results in Fig. 4(d) reveal the uniform distribution of those elements, which aligns well with the aforementioned SEM-based elemental mapping EDS results, providing additional confirmation of the primary chemical composition of the W, Mo-Ni<sub>3</sub>S<sub>2</sub>/NF electrode.

Furthermore, the XPS technique was adopted to analyze the elemental composition and bonding state of the electrode surface, and the analysis results are presented in Fig. 5. In the full spectrum of Fig. S4, the presence of Ni, S, W, Mo, C, and

oxygen (O) elements in the electrode can be clearly observed. The observed C and O peaks may arise from the organic compounds or atmospheric O<sub>2</sub> and CO<sub>2</sub> on the electrode surface. Fig. 5(a) displays the Ni 2p spectrum, revealing two Ni<sup>2+</sup> valence states, with peaks at about 855.3 eV and 873.4 eV correspond to Ni 2p<sub>3/2</sub> and Ni 2p<sub>1/2</sub>,<sup>25</sup> respectively. In addition, the peak at 852.5 eV is indexed to the metal Ni state.<sup>26</sup> The S 2p spectrum shown in Fig. 5(b) exhibits two peaks at 162.7 eV and 168.5 eV, which are attributed to S 2p<sub>1/2</sub> and SO<sub>x</sub>,<sup>27</sup> and corresponding to the Ni-S compound and surface oxidation of the S element, respectively. The spectrum of W 4f in Fig. 5(c) presents two peaks at 35.1 eV and 37.2 eV, which belong to W 4f<sub>7/2</sub> and W 4f<sub>5/2</sub>, respectively. In accordance with the pertinent literature,<sup>28,29</sup> W<sup>6+</sup> was present in the W, Mo-Ni<sub>3</sub>S<sub>2</sub>/NF electrocatalyst and combined to form WS<sub>2</sub>. Fig. 5(d) shows the high-resolution of the Mo 3d spectrum, where the binding energy peaks at 226.4 eV and 232.4 eV can be attributed to Mo 3d<sub>5/2</sub> and Mo 3d<sub>3/2</sub>, respectively, suggesting the existence of Mo<sup>4+</sup>. The other peak located at 235.3 eV was assigned to the oxidation of Mo (MoO<sub>x</sub>).<sup>30</sup> Notably, the binding energy of Ni 2p and Mo 3d exhibits slight positive shifts relative to their standard peaks (852.6 eV and 231.1 eV), while the binding energy of S 2p demonstrate a negative shift (164.0 eV). This phenomenon suggests an enhanced electron transfer capability of the

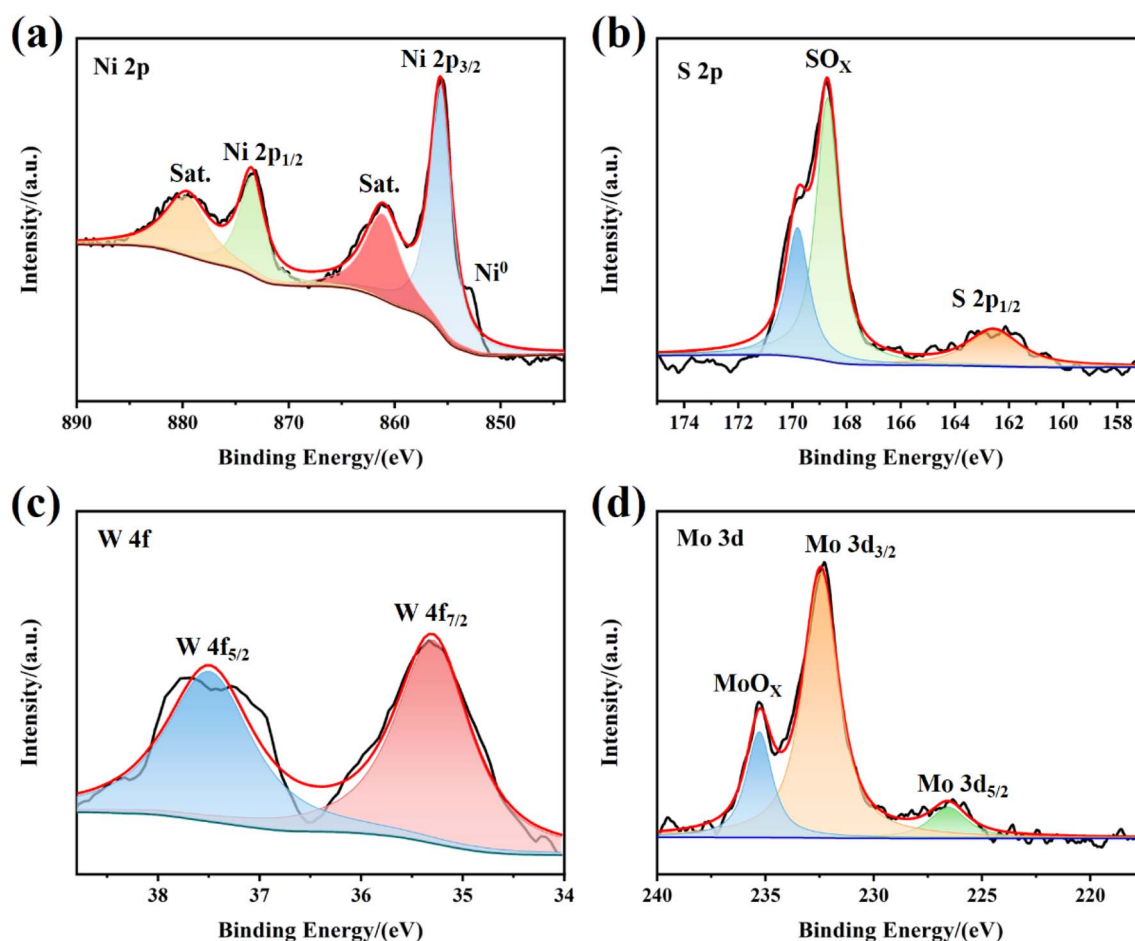


Fig. 5 The high-resolution XPS spectra of (a) Ni 2p, (b) S 2p, (c) W 4f and (d) Mo 3d of W, Mo-Ni<sub>3</sub>S<sub>2</sub>/NF electrode.



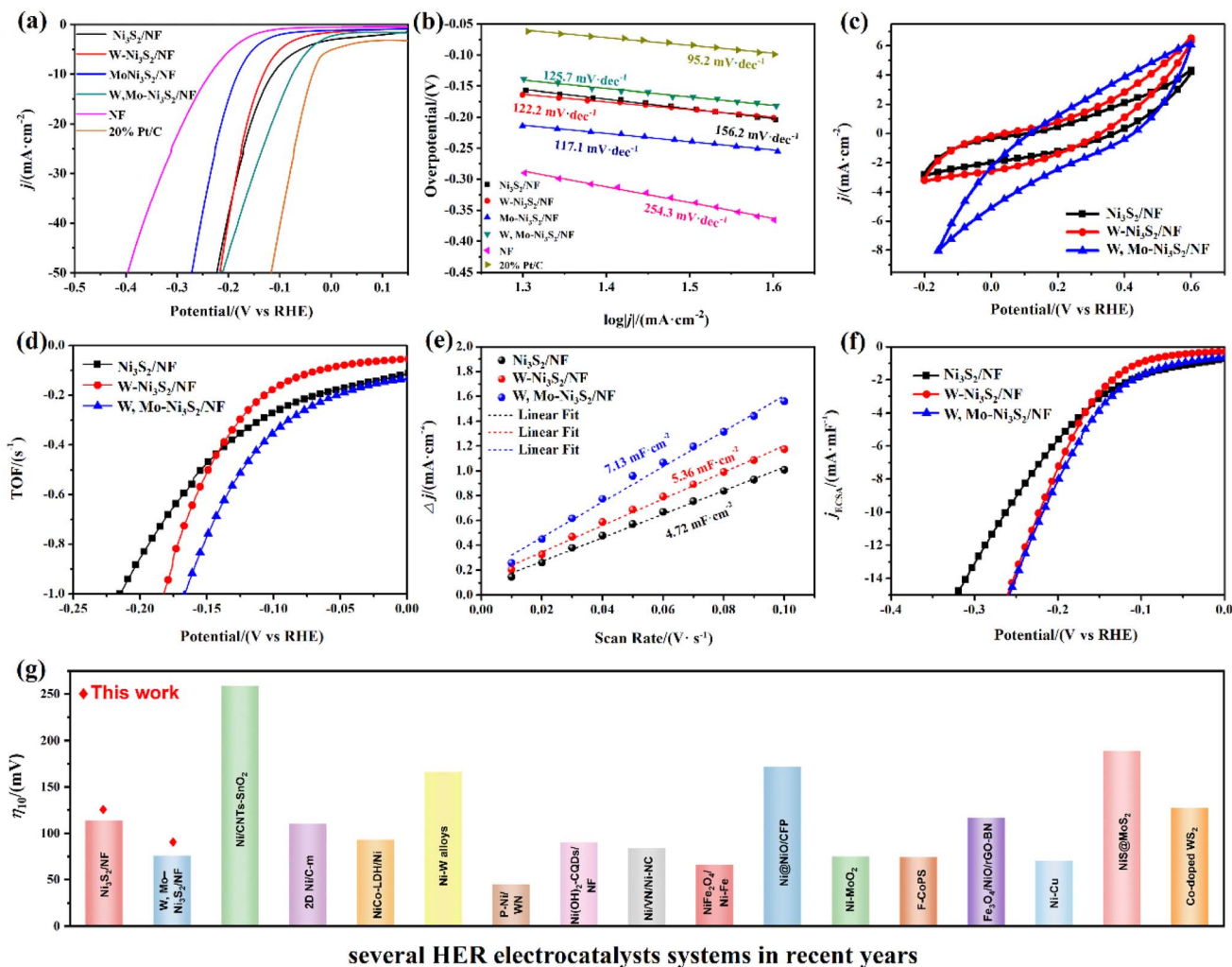


Fig. 6 Electrochemical properties of W, Mo-Ni<sub>3</sub>S<sub>2</sub>/NF electrodes. (a) Polarization curves; (b) Tafel fitting curves; (c) CV curves in PBS solution; (d) TOF vs. potential curves; (e) the linear plots of  $\Delta j$  vs. scanning rate and  $C_{dl}$  values; (f) normalized curves of  $j_{ECSA}$  vs. potential and (g) overpotential of W, Mo-Ni<sub>3</sub>S<sub>2</sub>/NF electrocatalyst compared with other non-noble catalysts reported in recent years.

Table 2 Comparison of HER activity of W, Mo-Ni<sub>3</sub>S<sub>2</sub>/NF and other non-noble catalysts

Electrode	Electrolyte	Current density (mA cm <sup>-2</sup> )	$\mu$ (mV)	Ref.
Ni <sub>3</sub> S <sub>2</sub> /NF	1 M KOH	10	114	This work
W, Mo-Ni <sub>3</sub> S <sub>2</sub> /NF	1 M KOH	10	76	This work
Ni/CNTs-SnO <sub>2</sub>	1 M KOH	10	259	32
2D Ni/C-m	1 M KOH	10	110	33
NiCo-LDH/Ni/NF	1 M KOH	10	93	34
Ni-W alloys	1 M KOH	10	166	35
P-Ni/WN	1 M KOH	10	45	36
Ni(OH) <sub>2</sub> -CQDs/NF	1 M KOH	10	90	37
Ni/VN/Ni-NC	1 M KOH	10	84	38
NiFe <sub>2</sub> O <sub>4</sub> /Ni-Fe	1 M KOH	10	66	39
Ni@NiO/CFP	1 M KOH	10	172	40
Ni-MoO <sub>2</sub>	1 M KOH	10	75	41
F-CoPS	1 M KOH	10	74	42
Fe <sub>3</sub> O <sub>4</sub> /NiO/rGO-BN	1 M KOH	10	117	43
Ni-Cu	1 M KOH	10	70	44
NiS@MoS <sub>2</sub>	1 M KOH	10	189	45
Co-doped WS <sub>2</sub>	1 M KOH	10	127	46



electrode, enabling easier electron transfer from Mo and Ni to S. Such behavior facilitates H adsorption and desorption during HER.<sup>26</sup> In the W, Mo-Ni<sub>3</sub>S<sub>2</sub>/NF electrode, the highly electronegative S atoms extract electrons from the metal sites, serving as active sites for stabilizing reaction intermediates. In addition, the active material Ni<sub>3</sub>S<sub>2</sub> forms an amorphous structure that is conducive to proton binding and electron transfer, accelerating charge transfer within the electrode and promoting electron accumulation on S atoms, enhancing the H evolution catalytic activity of the electrocatalyst.

The polarization curves of the Ni<sub>3</sub>S<sub>2</sub>/NF, W-Ni<sub>3</sub>S<sub>2</sub>/NF, Mo-Ni<sub>3</sub>S<sub>2</sub>/NF, and W, Mo-Ni<sub>3</sub>S<sub>2</sub>/NF electrodes are presented in Fig. 6(a). For comparison, the Pt/C electrode and NF substrate were also evaluated under identical conditions. Typically, a smaller HER overpotential correlates with lower energy

consumption during water electrolysis and better catalytic performance. The overpotential at 10 mA cm<sup>-2</sup> ( $\eta_{10}$ ) was employed as the evaluation criterion.<sup>31</sup> The Pt/C electrode exhibits exceptional H evolution performance, with an overpotential of only 36 mV. The W, Mo-Ni<sub>3</sub>S<sub>2</sub>/NF electrode also demonstrates excellent H evolution performance, achieving an overpotential of 76 mV at 10 mA cm<sup>-2</sup>. This value is 33.3%, 43.3%, and 58.5% lower than those of Ni<sub>3</sub>S<sub>2</sub>/NF (114 mV), W-Ni<sub>3</sub>S<sub>2</sub>/NF (134 mV), and Mo-Ni<sub>3</sub>S<sub>2</sub>/NF (183 mV), respectively. Table 2 and Fig. 6(g) summarize the overpotential of other similar non-noble metal catalysts at a current density of 10 mA cm<sup>-2</sup>. Evidently, the W, Mo-Ni<sub>3</sub>S<sub>2</sub>/NF electrocatalyst exhibits superior HER performance compared with other analogous non-noble metal catalysts. This enhanced performance can primarily be attributed to the synergistic catalytic effect

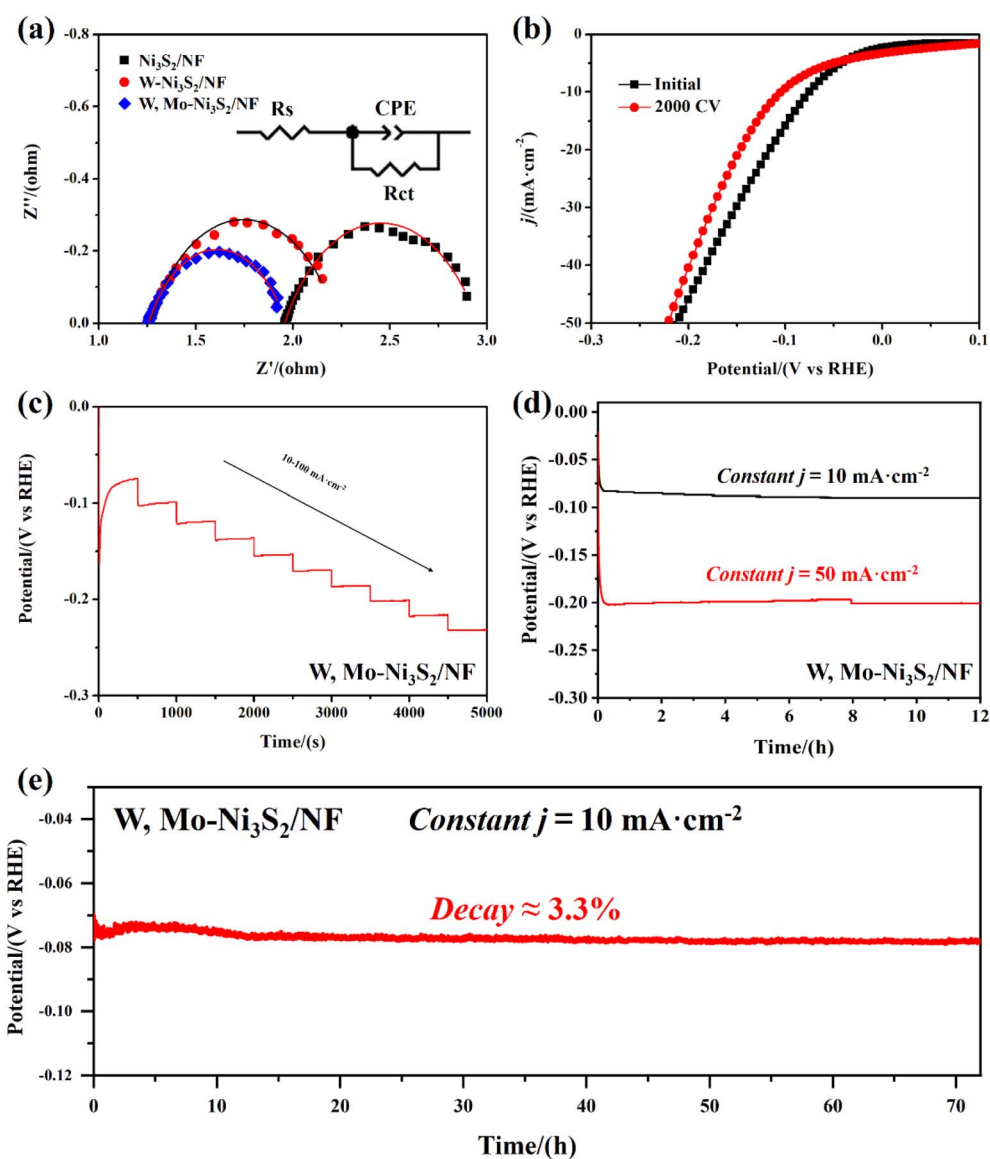


Fig. 7 (a) Nyquist plots of Ni<sub>3</sub>S<sub>2</sub>/NF, W-Ni<sub>3</sub>S<sub>2</sub>/NF, and W, Mo-Ni<sub>3</sub>S<sub>2</sub>/NF electrodes; (b) polarization curves before and after 2000 CV cycles, (c) multi-step chronopotentiometry curve, (d) chronopotentiometry curves at constant 10 and 50 mA cm<sup>-2</sup> and (e) 72 h chronopotentiometry curves at a 10 mA cm<sup>-2</sup> of W, Mo-Ni<sub>3</sub>S<sub>2</sub>/NF electrode.



between W and Mo doping and  $\text{Ni}_3\text{S}_2$ . In addition, the overpotential of  $\text{Ni}_3\text{S}_2/\text{NF}$  is lower than those of  $\text{W-Ni}_3\text{S}_2/\text{NF}$  and  $\text{Mo-Ni}_3\text{S}_2/\text{NF}$ . This phenomenon arises because W and Mo are co-deposited with Ni, reducing Ni content in the electrode, and thus, decreasing the amount of the active material  $\text{Ni}_3\text{S}_2$ , and consequently, reducing its activity.

Based on the Tafel equation:<sup>47</sup>  $\eta = a + b \log j$  (where  $\eta$  and  $j$  represent overpotential and current density, respectively,  $b$  is the Tafel slope, and  $a$  is a constant associated with temperature and pressure), the strong polarization regions of the polarization curves were linearly fitted, as depicted in Fig. 6(b). The resulting Tafel slopes for the  $\text{Ni}_3\text{S}_2/\text{NF}$ ,  $\text{W-Ni}_3\text{S}_2/\text{NF}$ ,  $\text{Mo-Ni}_3\text{S}_2/\text{NF}$ , and  $\text{W, Mo-Ni}_3\text{S}_2/\text{NF}$  electrodes were 156.2, 122.2, 117.1, and 125.7  $\text{mV dec}^{-1}$ , respectively. Compared with NF's Tafel slope of 254.3  $\text{mV dec}^{-1}$ , the electrodes prepared in this study exhibited significantly reduced Tafel slopes, indicating faster HER kinetics. Given the relatively inferior performance of the  $\text{Mo-Ni}_3\text{S}_2/\text{NF}$  electrode, its subsequent electrochemical data

were excluded from further analysis for a more intuitive understanding of the data and analysis.

The intrinsic catalytic activity of the electrodes was evaluated using turnover frequency (TOF). As shown in Fig. 6(c), the CV curves of different electrodes were measured in a phosphate buffered solution at pH = 7. In accordance with eqn (2):<sup>48</sup>

$$n = \frac{S}{2\mu F}, \quad (2)$$

$$\text{TOF} = \frac{J}{2nF}. \quad (3)$$

The calculated  $n$  values for the  $\text{Ni}_3\text{S}_2/\text{NF}$ ,  $\text{W-Ni}_3\text{S}_2/\text{NF}$ , and  $\text{W, Mo-Ni}_3\text{S}_2/\text{NF}$  electrodes were  $1.210 \times 10^{-4}$ ,  $1.508 \times 10^{-4}$ , and  $2.428 \times 10^{-4}$  mol, respectively. Based on these results, the TOF curves were derived by applying eqn (3) [see details in Fig. 6(d)]. At an overpotential of 150 mV, the TOF values of the  $\text{Ni}_3\text{S}_2/\text{NF}$ ,  $\text{W-Ni}_3\text{S}_2/\text{NF}$ , and  $\text{W, Mo-Ni}_3\text{S}_2/\text{NF}$  electrodes were 0.47, 0.51, and 0.77  $\text{s}^{-1}$ , respectively. These results indicate that the  $\text{W, Mo-Ni}_3\text{S}_2/\text{NF}$  electrode exhibits superior intrinsic catalytic activity and possesses more active sites for H evolution per unit area.

In addition to intrinsic catalytic activity, the overall catalytic performance of an electrode is also closely associated with its electrochemical active surface area (ECSA), where HERs occur on the electrode surface.<sup>49</sup> The CV curves of the electrodes in the non-faradaic region were measured at scan rates that ranged

**Table 3** Fitting results for  $\text{Ni}_3\text{S}_2/\text{NF}$ ,  $\text{W-Ni}_3\text{S}_2/\text{NF}$ , and  $\text{W, Mo-Ni}_3\text{S}_2/\text{NF}$  electrodes

Electrode	$R_s/(\Omega)$	$R_{ct}/(\Omega)$	CPE/(mF)
$\text{Ni}_3\text{S}_2/\text{NF}$	1.26	0.97	0.30
$\text{W-Ni}_3\text{S}_2/\text{NF}$	1.21	1.00	0.58
$\text{W, Mo-Ni}_3\text{S}_2/\text{NF}$	1.26	0.71	0.72

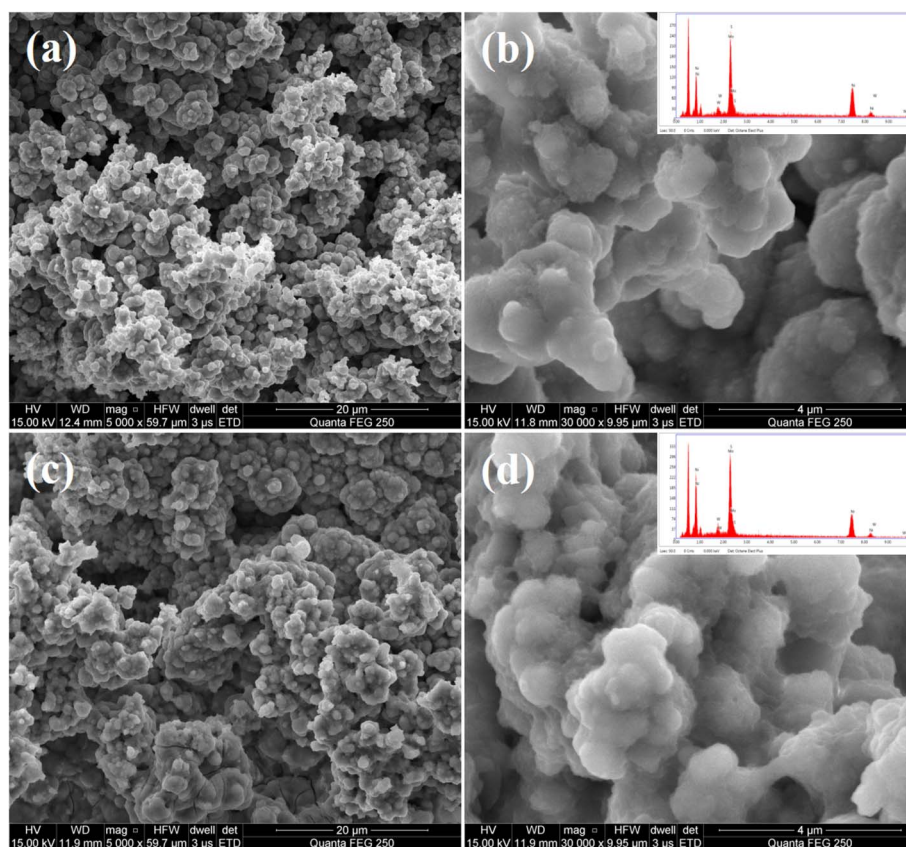


**Fig. 8** SEM images of  $\text{W, Mo-Ni}_3\text{S}_2/\text{NF}$  electrode; (a and b) initial and (c and d) after 2000 cycles.



from  $10 \text{ mV s}^{-1}$  to  $100 \text{ mV s}^{-1}$  (Fig. S5). A linear relationship was fitted between the current density difference  $\Delta j$  and scan rate. The slope of the resulting straight line corresponded to two times the  $C_{dl}$  value. As shown in Fig. 6(e), the  $C_{dl}$  values for the  $\text{Ni}_3\text{S}_2/\text{NF}$ ,  $\text{W-Ni}_3\text{S}_2/\text{NF}$ , and  $\text{W, Mo-Ni}_3\text{S}_2/\text{NF}$  electrodes are 4.72, 5.36, and  $7.13 \text{ mF cm}^{-2}$ , respectively. The cathodic polarization curves were normalized *via* ECSA, as depicted in Fig. 6(f). Under the same current density, the  $\text{W, Mo-Ni}_3\text{S}_2/\text{NF}$  electrode exhibited the lowest overpotential, indicating a significantly larger electrochemical active surface area. This finding corroborates the results obtained from the previous SEM analysis. By combining the above analyses, the superior catalytic activity of the  $\text{W, Mo-Ni}_3\text{S}_2/\text{NF}$  electrode can be attributed to its larger electrochemical active surface area and enhanced intrinsic catalytic activity.

Fig. 7(a) presents the Nyquist curves of the  $\text{Ni}_3\text{S}_2/\text{NF}$ ,  $\text{W-Ni}_3\text{S}_2/\text{NF}$ , and  $\text{W, Mo-Ni}_3\text{S}_2/\text{NF}$  electrodes measured at  $-100 \text{ mV}$  in  $1 \text{ M KOH}$ . The inset shows the equivalent circuit used for fitting, which includes resistance components, such as solution resistance ( $R_s$ ) and charge transfer resistance ( $R_{ct}$ ).<sup>50</sup> The

detailed fitting results are summarized in Table 3. As indicated in the table, the  $R_{ct}$  values of the  $\text{Ni}_3\text{S}_2/\text{NF}$ ,  $\text{W-Ni}_3\text{S}_2/\text{NF}$ , and  $\text{W, Mo-Ni}_3\text{S}_2/\text{NF}$  electrodes are 0.97, 1.00, and  $0.71 \Omega$ , respectively. These results indicate that the  $\text{W, Mo-Ni}_3\text{S}_2/\text{NF}$  electrode exhibits better electrical conductivity and faster charge transfer rate due to faster charge migration during the HER process.

The stability of the H evolution electrode serves as a critical parameter for assessing its performance. Fig. 7(b) illustrates the polarization curves of the  $\text{W, Mo-Ni}_3\text{S}_2/\text{NF}$  electrode before and after 2000 CV cycles (scan range:  $0 \text{ mV}$  to  $-300 \text{ mV}$  *versus* RHE, scan rate:  $100 \text{ mV s}^{-1}$ ). The results indicate that the H evolution activity of the  $\text{W, Mo-Ni}_3\text{S}_2/\text{NF}$  electrode exhibits only a minor reduction. As shown in Fig. 7(c), the multistep electrolysis curves under current density that ranges from  $10 \text{ mA cm}^{-2}$  to  $100 \text{ mA cm}^{-2}$  demonstrate a steady and incremental increase in potential with increasing current density, highlighting the excellent mass transfer capability and mechanical robustness of the  $\text{W, Mo-Ni}_3\text{S}_2/\text{NF}$  electrode. Furthermore, Fig. 7(d) presents the CP curves of the  $\text{W, Mo-Ni}_3\text{S}_2/\text{NF}$  electrode in  $1.0 \text{ M KOH}$ . Under a constant current density of  $10 \text{ mA cm}^{-2}$  and  $50 \text{ mA cm}^{-2}$ , the electrode maintains stable operation for 12 h, with minimal fluctuations in the potential. Furthermore, the 72 h long-term constant current electrolysis test in Fig. 7(e) demonstrated that the potential decay was merely approximately 3.3%, which not only corroborates the data presented in Fig. 7(d) but also suggests that the electrode possesses promising potential for practical applications. These findings confirm that the  $\text{W, Mo-Ni}_3\text{S}_2/\text{NF}$  electrocatalyst developed in the current study

Table 4 Elemental composition of the  $\text{W, Mo-Ni}_3\text{S}_2/\text{NF}$  electrode before and after 2000 CV cycles

Electrode	Ni/(wt%)	S/(wt%)	W/(wt%)	Mo/(wt%)
Initial	69.15	14.98	6.40	9.47
After 2000CV	70.88	14.55	5.68	8.89

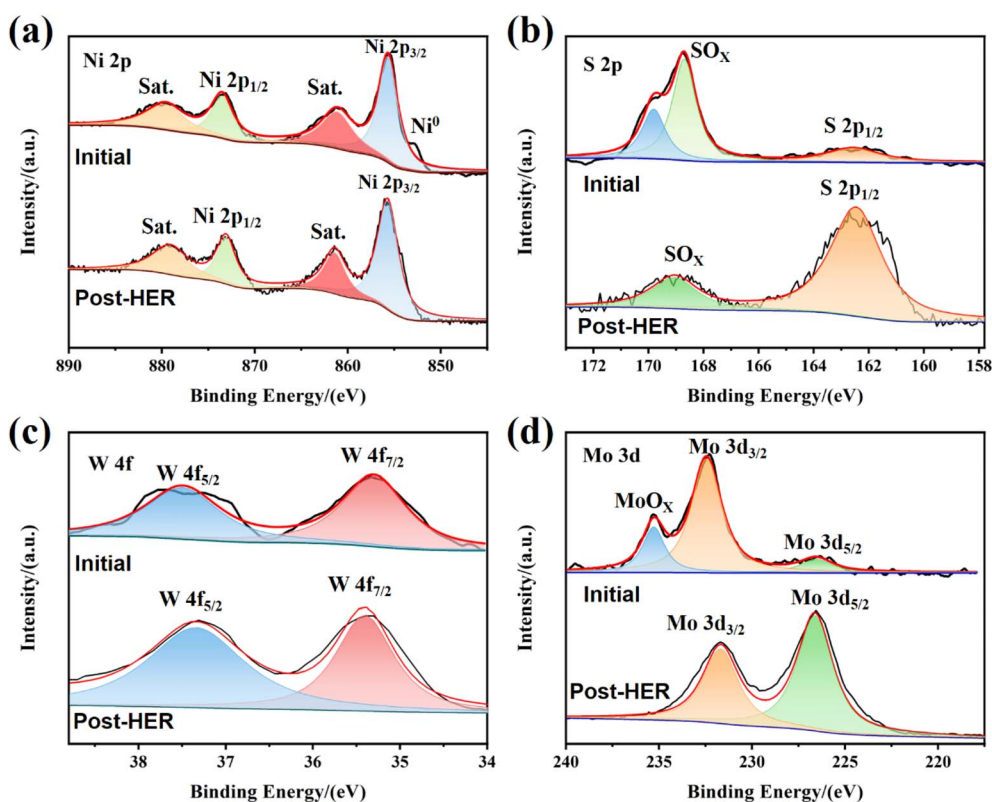


Fig. 9 XPS characterization of  $\text{W, Mo-Ni}_3\text{S}_2/\text{NF}$  before and after 2000 CV test. (a) Ni 2p, (b) S 2p, (c) W 4f and (d) Mo 3d.



possesses remarkable stability and durability. The SEM images and elemental composition analysis of the W, Mo-Ni<sub>3</sub>S<sub>2</sub>/NF electrode before and after 2000 CV cycles are displayed in Fig. 8 and Table 4, respectively. After electrolysis, cracks are observed in certain regions of the electrode surface, accompanied by a reduction in the number of cellular structures and smoother interconnections. The data presented in the table indicate a decrease in the contents of both W and Mo. This suggests that the observed morphological changes may be associated with the dissolution of W and Mo elements. Nevertheless, the electrode largely retained its original morphology after 2000 CV cycles, indicating its good electrochemical stability. Fig. 9 displays the XPS spectra of the W, Mo-Ni<sub>3</sub>S<sub>2</sub>/NF electrocatalyst before and after 2000 CV cycles to examine changes in elemental states. In the Ni 2p spectrum, the characteristic binding energy peak associated with metallic Ni vanishes after cycling, indicating that Ni<sup>0</sup> is oxidized and dissolved during the HER process in electrolyte environment. Concurrently, a notable increase in the binding energy of the S 2p<sub>1/2</sub> peak is observed, suggesting that sulfur species may have undergone electron gain, potentially forming reduced sulfur intermediates or stabilizing higher oxidation states through charge redistribution. For W 4f, an increased relative intensity of the W 4f<sub>5/2</sub> component is evident, reflecting a rise in the proportion of W<sup>6+</sup>,<sup>51</sup> likely due to surface oxidation under HER processes. Similarly, for Mo 3d, the disappearance of the Mo-O related peak (MoOx) accompanied by an enhanced Mo 3d<sub>5/2</sub> signal indicates a transformation of molybdenum into the Mo<sup>6+</sup> state, consistent with oxidative conversion during prolonged electrochemical cycling.<sup>52</sup>

## 4. Conclusion

The self-supported W, Mo-Ni<sub>3</sub>S<sub>2</sub>/NF electrode prepared *via* one-step constant current electrodeposition on NF substrate demonstrates remarkable H evolution activity, exhibiting an overpotential of 76 mV at a current density of 10 mA cm<sup>-2</sup> and a Tafel slope of 125.7 mV dec<sup>-1</sup>. This phenomenon can be attributed to the following factors: (1) morphologically, the refined spherical particles and roughened surface enhance the contact area with the electrolyte, providing a significantly larger active surface area for the reaction. (2) In terms of phase and elemental composition, the coexistence of crystalline and amorphous structures introduces abundant structural defects, exposing more active centers and unsaturated sites that facilitate catalytic activity. (3) From the perspective of electron distribution, the incorporation of W and Mo modifies the electronic structure, enabling the highly electronegative S atoms to more effectively absorb electrons from metal sites, forming stable reaction intermediates, which not only accelerate the charge transfer rate but also promote the accumulation of electrons on S atoms, significantly enhancing the H evolution catalytic performance of the electrocatalyst.

## Author contributions

Wenyu Tan: writing – review & editing, writing – original draft, formal analysis, data curation, conceptualization. Hanwei He:

validation, supervision, project administration, funding acquisition.

## Conflicts of interest

The authors declare that they have no known competing financial interests or personal relationships that could have appeared to influence the work reported in this paper.

## Data availability

The data that support the findings of this study are available from the corresponding author HW. He, upon reasonable request.

Supplementary information is available. See DOI: <https://doi.org/10.1039/d5ra07318a>.

## Acknowledgements

Authors very thanks for the help from the friends and the authoritative opinion and suggestions from the reviews.

## References

- 1 T. T. Le, P. Sharma, B. J. Bora, V. D. Tran, T. H. Truong, H. C. Le and P. Q. P. Nguyen, Fueling the future: A comprehensive review of hydrogen energy systems and their challenges, *Int. J. Hydrogen Energy*, 2024, **54**, 791–816.
- 2 H. Tüysüz, Alkaline water electrolysis for green hydrogen production, *Acc. Chem. Res.*, 2024, **57**, 558–567.
- 3 C. Wang, W. Guo, T. Chen, W. Lu, Z. Song, C. Yan, Y. Feng, F. Gao, X. Zhang and Y. Rao, Advanced noble-metal/transition-metal/metal-free electrocatalysts for hydrogen evolution reaction in water-electrolysis for hydrogen production, *Coord. Chem. Rev.*, 2024, **514**, 215899.
- 4 Y. Chen, Y. Fan, Z. Cui, H. Huang, D. Cai, J. Zhang, Y. Zhou, M. Xu and R. Tong, Nickel sulfide-based electrocatalysts for overall water splitting, *Int. J. Hydrogen Energy*, 2023, **48**, 27992–28017.
- 5 M. Mahanthappa, M. P. Bhat and A. Alshoaibi, Exploring the role of redox-active species on NiS-NiS<sub>2</sub> incorporated sulfur-doped graphitic carbon nitride nanohybrid as a bifunctional electrocatalyst for overall water splitting, *Int. J. Hydrogen Energy*, 2024, **84**, 641–649.
- 6 A. Fathollahi, T. Shahrabi and G. B. Darband, Modulation of active surface sites on Ni-Fe-S by the dynamic hydrogen bubble template method for energy-saving hydrogen production, *J. Mater. Chem. A*, 2024, **12**, 9038–9054.
- 7 J. A. Bau, S. M. Kozlov, L. M. Azofra, S. Ould-Chikh, A.-H. Emwas, H. Idriss, L. Cavallo and K. Takanabe, Role of oxidized Mo species on the active surface of Ni-Mo electrocatalysts for hydrogen evolution under alkaline conditions, *ACS Catal.*, 2020, **10**, 12858–12866.
- 8 M. Jakšić, Electrocatalysis of hydrogen evolution in the light of the brewer-engel theory for bonding in metals and intermetallic phases, *Electrochim. Acta*, 1984, **29**, 1539–1550.



- 9 M. M. Jaksic, Interionic nature of synergism in catalysis and electrocatalysis, *Solid State Ionics*, 2000, **136**, 733–746.
- 10 N. Yang, Z. Chen, D. Ding, C. Zhu, X. Gan and Y. Cui, Tungsten–nickel alloy boosts alkaline hydrogen evolution reaction, *J. Phys. Chem. C*, 2021, **125**, 27185–27191.
- 11 S. Sekar, S. B. Devi, S. Maruthasalamoorthy, T. Maiyalagan, D. Y. Kim, S. Lee and R. Navamathavan, One-step facile hydrothermal synthesis of rGO-CoS<sub>2</sub> nanocomposites for high performance HER electrocatalysts, *Int. J. Hydrogen Energy*, 2022, **47**, 40359–40367.
- 12 M. Al-Mamun, Y. Wang, P. Liu, Y. L. Zhong, H. Yin, X. Su, H. Zhang, H. Yang, D. Wang and Z. Tang, One-step solid phase synthesis of a highly efficient and robust cobalt pentlandite electrocatalyst for the oxygen evolution reaction, *J. Mater. Chem. A*, 2016, **4**, 18314–18321.
- 13 I. El-Hallag, S. Elsharkawy and S. Hammad, The effect of electrodeposition potential on catalytic properties of Ni nanoparticles for hydrogen evolution reaction (HER) in alkaline media, *J. Appl. Electrochem.*, 2022, **52**, 907–918.
- 14 F. J. Vidal-Iglesias, J. Solla-Gullón, A. Rodes, E. Herrero and A. Aldaz, Understanding the Nernst equation and other electrochemical concepts: an easy experimental approach for students, *J. Chem. Educ.*, 2012, **89**, 936–939.
- 15 J. Hu, S. Li, Y. Li, J. Wang, Y. Du, Z. Li, X. Han, J. Sun and P. Xu, A crystalline–amorphous Ni–Ni (OH)<sub>2</sub> core–shell catalyst for the alkaline hydrogen evolution reaction, *J. Mater. Chem. A*, 2020, **8**, 23323–23329.
- 16 X. Lv, P. Kannan, S. Ji, X. Wang and H. Wang, Synthesis of Ni<sub>3</sub>S<sub>2</sub> catalysts using various sulphur sources and their HER and OER performances, *CrystEngComm*, 2020, **22**, 6517–6528.
- 17 J. Zhang, T. Wang, D. Pohl, B. Rellinghaus, R. Dong, S. Liu, X. Zhuang and X. Feng, Interface engineering of MoS<sub>2</sub>/Ni<sub>3</sub>S<sub>2</sub> heterostructures for highly enhanced electrochemical overall-water-splitting activity, *Angew. Chem.*, 2016, **128**, 6814–6819.
- 18 H. Kim, H. Park, D.-K. Kim, S. Oh, I. Choi and S.-K. Kim, Electrochemically fabricated NiW on a Cu nanowire as a highly porous non-precious-metal cathode catalyst for a proton exchange membrane water electrolyzer, *ACS Sustain. Chem. Eng.*, 2019, **7**, 8265–8273.
- 19 J. Zhang, J. Lian, Q. Jiang and G. Wang, Boosting the OER/ORR/HER activity of Ru-doped Ni/Co oxides heterostructure, *Chem. Eng. J.*, 2022, **439**, 135634.
- 20 Z. Wang, S. Shen, Z. Lin, W. Tao, Q. Zhang, F. Meng, L. Gu and W. Zhong, Regulating the local spin state and band structure in Ni<sub>3</sub>S<sub>2</sub> nanosheet for improved oxygen evolution activity, *Adv. Funct. Mater.*, 2022, **32**, 2112832.
- 21 E. Aslan, A. Sarilmaz, G. Yanalak, C. S. Chang, I. Cinar, F. Ozel and I. H. Patir, Facile preparation of amorphous NiWSex and CoWSex nanoparticles for the electrocatalytic hydrogen evolution reaction in alkaline condition, *J. Electroanal. Chem.*, 2020, **856**, 113674.
- 22 J. Jakšić, M. Vojnović and N. V. Krstajić, Kinetic analysis of hydrogen evolution at Ni–Mo alloy electrodes, *Electrochim. Acta*, 2000, **45**, 4151–4158.
- 23 S. He, L. Liu, Y. Yang, W. Liu, W. Tan and C. Zhou, Enhanced hydrogen evolution in alkaline media by electrodeposition of floral spherical Ni–Se–Yb/NF electrocatalyst, *Fuel*, 2025, **382**, 133744.
- 24 J. G. L. Tao, J. Chen, B. Zhao, R. Feng, M. Shakouri and F. Chen, Ni<sub>3</sub>C/Ni<sub>3</sub>S<sub>2</sub> Heterojunction Electrocatalyst for Efficient Methanol Oxidation via Dual Anion Co-modulation Strategy, *Small*, 2024, **20**, 2402492.
- 25 M. Zhou, Y. Liu, D. Fa, L. Qian and Y. Miao, Growth of radial microspheres of Ni–Co–O at porous Ti and its phosphorization for high efficient hydrogen evolution, *Electrochim. Acta*, 2018, **259**, 329–337.
- 26 S. Liu, Q. Jin, Y. Xu, X. Fang, N. Liu, J. Zhang, X. Liang and B. Chen, The synergistic effect of Ni promoter on Mo–S/CNT catalyst towards hydrodesulfurization and hydrogen evolution reactions, *Fuel*, 2018, **232**, 36–44.
- 27 B. Zhang, J. Liu, J. Wang, Y. Ruan, X. Ji, K. Xu, C. Chen, H. Wan, L. Miao and J. Jiang, Interface engineering: The Ni (OH)<sub>2</sub>/MoS<sub>2</sub> heterostructure for highly efficient alkaline hydrogen evolution, *Nano Energy*, 2017, **37**, 74–80.
- 28 M. Tong, L. Wang, P. Yu, C. Tian, X. Liu, W. Zhou and H. Fu, Ni<sub>3</sub>S<sub>2</sub> nanosheets in situ epitaxially grown on nanorods as high active and stable homojunction electrocatalyst for hydrogen evolution reaction, *ACS Sustain. Chem. Eng.*, 2018, **6**, 2474–2481.
- 29 T. Van Nguyen, M. Tekalgne, T. P. Nguyen, Q. Van Le, S. H. Ahn and S. Y. Kim, Electrocatalysts based on MoS<sub>2</sub> and WS<sub>2</sub> for hydrogen evolution reaction: An overview, *Battery Energy*, 2023, **2**, 20220057.
- 30 L. Jinlong, G. Wenli, L. Tongxiang, S. Ken and M. Hideo, Improving hydrogen evolution reaction for MoS<sub>2</sub> hollow spheres, *J. Electroanal. Chem.*, 2017, **799**, 304–307.
- 31 N. Bhuvanendran, S. Ravichandran, Q. Xu, T. Maiyalagan and H. Su, A quick guide to the assessment of key electrochemical performance indicators for the oxygen reduction reaction: A comprehensive review, *Int. J. Hydrogen Energy*, 2022, **47**, 7113–7138.
- 32 L. Xing, Y. Hao, Y. Wang, Y. Zhao, Y. Zuo and C. Sun, Microstructure and Hydrogen Evolution Catalytic Properties of Ni/CNTs–SnO<sub>2</sub> Prepared by Electrodeposition Method, *Russ. J. Phys. Chem. A*, 2025, **99**, 318–326.
- 33 H. Ke, Y. Xie, Y. Luo, Y. Gao, L. Yin, J. Fu and L. Chen, Novel one-step solid-state synthesis of 2D Ni/C for efficient electro/photo-catalytic hydrogen evolution, *Fuel*, 2025, **393**, 135067.
- 34 Y. Sun, S. Zhou, N. Yang, H. Shen, X. Yang, L. Zhang, X. Xiao, B. Jiang and L. Zhang, Constructing NiCo-hydroxide/Ni Mott–Schottky heterostructure electrocatalyst for enhanced alkaline hydrogen evolution reaction by inducing interfacial electron redistribution, *J. Colloid Interface Sci.*, 2025, **688**, 1–10.
- 35 Y. Li, L. Li, W. Li, L. Lu, L. Tian, Y. Liu, C. Su and W. Tian, Preparation of Porous Ni–W Alloys Electrodeposited by Dynamic Hydrogen Bubble Template and Their Alkaline HER Properties, *Coatings*, 2024, **14**, 957.
- 36 S. Liang, P. Wang, M. Jing, H. Hu, S. Zhang, Z. Cang, Y. Zhao, H. Gong and J. Liu, Nickel Nanoparticles Supported on P-Doped Tungsten Nitride Nanosheets as Catalysts for



- Hydrogen Evolution, *ACS Appl. Nano Mater.*, 2024, 7, 11553–11559.
- 37 Y. Cong, Q. Zheng, X. Wang, X. Li, Q. Zheng and S.-W. Lv, In-situ generated CQDs-doped Ni (OH)<sub>2</sub> nanosheets with high photoelectric activity on nickel foam for efficient hydrogen evolution reaction in alkaline solution, *Int. J. Hydrogen Energy*, 2024, 70, 71–78.
- 38 Q. Liu, K. Liu, X. Li, C. Hui, J. Huang, Z. Deng, D. Yang, L. Cao and L. Feng, Ni and VN Nanoparticles Supported on N-Doped Carbon Layer Containing Ni Single Atoms as Electrocatalyst for the Hydrogen Evolution Reaction, *ACS Appl. Nano Mater.*, 2024, 7, 4059–4067.
- 39 W. Wang, W. Yang, R. Xu, S. Feng and X. Wang, The mechanism of enhanced electrocatalytic water splitting on S-doped NiFe<sub>2</sub>O<sub>4</sub>/Ni-Fe alloy@ copper foams, *Nanotechnology*, 2024, 35, 365702.
- 40 R. Li, Z. Pu, R. Zhou, Y. Li, Y. Huang, S. Li, J. Yang, D. Zhang and M. Pi, In situ controllable construction of Ni@NiO Schottky heterojunctions for electrocatalytic hydrogen evolution, *J. Mater. Chem. C*, 2024, 12, 18849–18855.
- 41 L. Li, J. Chen, Z. Xiao, X. Zhang, S. K. Kwak, D. Tian and J. M. Lee, Coupled Lattice-Expanded Ni and MoO<sub>2</sub> Array for Efficient Alkaline Hydrogen Evolution, *Adv. Sustainable Syst.*, 2024, 2400587.
- 42 Z. Dai, B. Wang, W. Li, Y. Wu, B. Yan and K. Zhang, Synergistic effects of fluorine doping on CoPS electrocatalysts for highly efficient hydrogen evolution reaction, *RSC Adv.*, 2025, 15, 9756–9762.
- 43 N. Baby, S. Thangarasu, N. Murugan, Y. A. Kim and T.-H. Oh, MOF derived Fe<sub>3</sub>O<sub>4</sub>/NiO decorated rGO-BN for efficient electrochemical water splitting, *Int. J. Hydrogen Energy*, 2025, 130, 127–138.
- 44 S. Skakri, A. El Attar, S. Benhaiba, B. Bouljoihel, A. Aaddane, A. Mouakkar, A. Rais and M. El Rhazi, Facile synthesis of a Ni-Cu composite reinforced with a para-phenylenediamine layer for enhanced hydrogen evolution reaction, *RSC Adv.*, 2025, 15, 24256–24269.
- 45 G. E. O. Nsang, B. Ullah, S. Hua, S. A. Shah, N. Ullah, N. Ullah, F. N. Dike, W. Yaseen, A. Yuan and N. Khan, NiS nanoparticle-MoS<sub>2</sub> nanosheet core-shell spheres: PVP-assisted synthesis and efficient electrocatalyst for hydrogen evolution reaction, *Energy Mater.*, 2025, 5, 500047.
- 46 A. Thennarasi and K. Vasu, Co-degenerate doped WS<sub>2</sub> electrocatalyst with enriched CoS phase producing efficient hydrogen evolution at all pH conditions, *J. Power Sources*, 2025, 657, 238241.
- 47 C. Kong, Y.-X. Han, L.-j. Hou and P.-J. Yan, The distribution effect of sulfur vacancy in 2H-MoS<sub>2</sub> monolayer on its H<sub>2</sub> generation mechanism from density functional theory, *Int. J. Hydrogen Energy*, 2022, 47, 242–249.
- 48 T. Liu, W. Gao, Q. Wang, M. Dou, Z. Zhang and F. Wang, Selective loading of atomic platinum on a RuCeOx support enables stable hydrogen evolution at high current densities, *Angew. Chem.*, 2020, 132, 20603–20607.
- 49 C. Wei, S. Sun, D. Mandler, X. Wang, S. Z. Qiao and Z. J. Xu, Approaches for measuring the surface areas of metal oxide electrocatalysts for determining their intrinsic electrocatalytic activity, *Chem. Soc. Rev.*, 2019, 48, 2518–2534.
- 50 Y. Choquette, L. Brossard, A. Lasia and H. Menard, Study of the kinetics of hydrogen evolution reaction on raney nickel composite-coated electrode by AC impedance technique, *J. Electrochem. Soc.*, 1990, 137, 1723.
- 51 S. Chen, J. Zhang, C. Xu, X. Tan, J. Liang and Y. Guo, Practical Monolithic W, Mo Dual-Doped NiFeB Catalyst for Overall Water Splitting, *ACS Appl. Energy Mater.*, 2025, 8, 7583–7593.
- 52 X. He, Y. Li, J. Yang, G. Zeng and L. Wu, Co-deposition of Ni-Mo alloy film catalysts for hydrogen evolution from an ethylene glycol system, *RSC Adv.*, 2024, 14, 34165–34174.

